Covalency-Driven Structural Evolution in the Polar Pyrochlore Series $Cd_2Nb_2O_{7-x}S_x$

Geneva Laurita,[*,†] Daniel Hickox-Young,[‡] Samra Husremovic,[†] Jun Li,[¶] Arthur W. Sleight,[¶] Robin Macaluso,[§] James M. Rondinelli,[‡] and Mas A. Subramanian[¶]

†*Department of Chemistry and Biochemistry, Bates College, Lewiston, ME*

‡*Department of Materials Science and Engineering, Northwestern University, Evanston, IL*

¶*Department of Chemistry, Oregon State University, Corvallis, OR*

§*Department of Chemistry and Biochemistry, University of Texas at Arlington, Arlington, TX*

E-mail: glaurita@bates.edu

Abstract

The arrangement of cations on the triangular pyrochlore lattice leads to a wealth of interesting physical phenomena influenced by geometric frustration. Although uncommon, several pyrochlore materials overcome this frustration and exhibit polar structures. Unraveling the origin of such behavior is key to understanding how broken inversion symmetry arises in complex crystal structures. Here we investigate the effect of varying degrees of covalency in the pyrochlore lattice through a detailed structural and lattice dynamical analysis of the pyrochlore oxysulfide series $Cd_2Nb_2O_{7-x}S_x$ above and below the ferroelectric transition temperatures (T_C) using synchrotron x-ray diffraction (SXRD) and first principles calculations. All compositions exhibit the cubic $Fd\bar{3}m$ pyrochlore aristotype above T_C, whereas the amplitude and character of various structural distortions are found to be composition dependent below T_C. For $x = 0$, large Cd and Nb cation displacements occur to produce the polar $Ima2$ structure accompanied by a change in translational symmetry. Our symmetry and lattice dynamical calculations indicate $Cd_2Nb_2O_7$ undergoes a proper ferroelectric transition through T_C. Analysis of the sulfur-substituted niobates indicates that although the polar space group $Fdd2$ is adopted by the nominal $x = 0.25$ sample, the transition into the polar phase is improper. For the nominally $x = 0.7$ composition, the lattice remains nearly cubic, but exhibits a high degree of structural disorder in the pyrochlore channel, with a deviation from the linear Cd-X'-Cd bond by nearly 15 ° to accommodate the large size of S while preventing extreme stretching of the Nb–O bond. This highly distorted Cd–X' network is accompanied by a highly distorted NbO_6 network, which is accommodated by the polarizable NbO_6 coordination environment. This sheds light on the limited existence of oxysulfide pyrochlores, for example, the lack of reported S substitution in the case of the similar yet less-polarizable $Cd_2Ta_2O_7$. Our work both provides new understanding of how inversion-symmetry lifting displacements arise and how anion substitution, which tunes covalent cation-anion interactions, is a useful strategy for manipulating polar behavior in the pyrochlore lattice.

Introduction

Ferroelectricity is well known and understood in perovskite materials such as $BaTiO_3$ and $PbTiO_3$, but very few pyrochlores exhibit this phenomenon. While the pyrochlore structure supports numerous chemical compositions, various forms of ferroelectricity (proper, improper, relaxor, etc.) have only been reported in $Cd_2Nb_2O_7$[1] and related compounds,[2] $Ho_2Ti_2O_7$,[3,4] $La_2Zr_2O_7$,[5] $Nd_2Ti_2O_7$,[6] and frustrated ferroelectricity in $Y_2(Nb_{0.86}Y_{0.14})_2O_{6.91}$, $CaYNb_2O_7$, and Y_2NbTiO_7.[7] Many of these studies illustrate the complex behavior of the pyrochlore lattice upon cooling, and unlike perovskite-structured compounds, the origin of coherent polar displacements in pyrochlore oxides is not well understood.

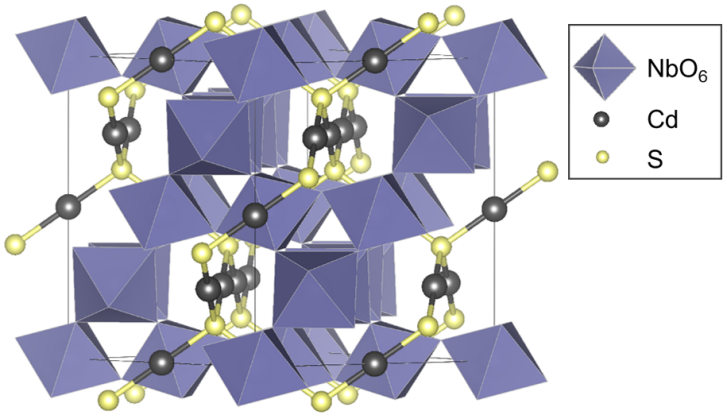

Figure 1: Illustration of the ideal cubic $Fd\bar{3}m$ pyrochlore $Cd_2Nb_2O_6S$ with Cd on the 16*d* Wyckoff site at ($\frac{1}{2}$, $\frac{1}{2}$, $\frac{1}{2}$), Nb on the 16*c* Wyckoff site at (0, 0, 0), O on the 48*f* Wyckoff site at (x, $\frac{1}{8}$, $\frac{1}{8}$), and S on the 8*b* Wyckoff site at ($\frac{3}{8}$, $\frac{3}{8}$, $\frac{3}{8}$).

The complex nature of the pyrochlore structure arises from the greater number of sites and geometries that the atoms can occupy in relation to the perovskite structure. The structure is commonly described as two interpenetrating sublattices of corner-shared BO_6 octahedra and A_2O' chains, illustrated in Figure 1.[8,9] The general structure can be written as $A_2B_2O_6O$', as the oxygen atoms in the structure are found on two distinct crystallographic Wyckoff sites: the BO_6 oxygen atoms are located at the (x, $\frac{1}{8}$, $\frac{1}{8}$) 48*f* site while the A_2O' oxygen is located at the ($\frac{3}{8}$, $\frac{3}{8}$, $\frac{3}{8}$) 8*b* site. The pyrochlore structure can host a large array of

cation and anion substitution,[2,10–13] in addition to tolerating cation and anion vacancies and structural and site disorder.[14–20] However, structural distortions such as cation off-centering are frustrated in the pyrochlore structure due to the triangular arrangement of cations on the lattice,[21–23] inhibiting a transition from a paraelectric to ferroelectric phase in majority of pyrochlore oxide materials.

Ferroelectricity was first observed in $Cd_2Nb_2O_7$ in 1952;[1] thereafter a ferroelectric transition temperature of 185 K was confirmed.[24,25] Since its discovery, numerous studies have been carried out on this material, and the oftentimes conflicting nature of the reports is a reflection of the underlying structural complexity. A combination of sharp and diffuse signatures in the structure and property measurements upon cooling have led to various conclusions of the ferroelectric nature of the material, from the superposition of improper and proper ferroelectric transitions[26] to relaxor-like behavior.[27,28] The material undergoes a phase transition at approximately 204 K, evidenced by small peaks in heat capacity and dielectric measurements.[29] This has been described as a second order[29] and improper ferroelastic[26] as well as an improper ferroelectric[30] transition, with reports of tetragonal,[31] orthorhombic,[32] and rhombohedral[33] crystal structures. In addition, a series of phase transitions have been observed around 190 K, leading to conclusions of relaxor behavior due to broad signatures in the heat capacity and dielectric data.[29] Infrared[26] and Raman[34] measurements indicate second-order behavior around this temperature, adding to the complexity of the literature surrounding this transition temperature. There are two further phase transitions reported at approximately 85 K to an uncharacterized monoclinic phase, and the fourth at approximately 45 K to another unique monoclinic phase.[35–37] Although there is a large amount of literature on the structural characterization of $Cd_2Nb_2O_7$, the vast majority of the analysis is on single crystal samples,[26–28,32,33,35–39] and the propensity towards twinning in these crystals necessitates the analysis of high resolution powder diffraction data. There are a few reports of powder analysis, but the conflicting identified phases of $Ima2$ (#46)[31] and $I\bar{4}m2$ (#119)[40] justify the need for further analysis of powder data.

$Cd_2Nb_2O_6S$ and a solid solution $Cd_2Nb_2O_{7-x}S_x$ ($x = 0$–1) were reported to exhibit acentricity through second harmonic generation,[2] and the origin of polarity across the solid solution was attributed to dynamic displacement of the Cd^{2+} cations.[41,42] A total of four phase transitions were determined in the solid solution (labeled as α, β, γ, and δ), but detailed characterization of the space groups and atomic positions of the low temperature phases were not reported. The lack of literature on the low-temperature structure of the solid solution $Cd_2Nb_2O_{7-x}S_x$ may be a result of the complex patterns that are seen upon phase transformations. In order to observe well-resolved phase transitions, high-resolution powder diffraction is needed. As Cd is a strong absorber of neutron radiation, X-ray synchrotron radiation is the best alternative source to provide the necessary resolution. Herein we present work on the structural characterization of the ferroelectric pyrochlore series $Cd_2Nb_2O_{7-x}S_x$ ($x = 0 - 0.7$) through synchrotron diffraction experiments coupled with first principles calculations to assess the cooperative diplacements active through the parity-lifting transitions. We find that the sulfur concentration changes the nature of the phase transitions and the symmetries exhibited by the low-temperature structures. We attribute these variations in the oxysulfide to changes in the cation-anion bond covalency and polarizability in the pyrochlore lattice. This work contributes to the understanding of polar phases in pyrochlore materials, helping to elucidate mechanisms which may be applied to other mixed-anion pyrochlores.

Experimental

Sample Preparation and Characterization

Polycrystalline samples of $Cd_2Nb_2O_{7-x}S_x$ ($x = 0$, 0.25, and 0.7) were prepared by mixing a stoichiometric ratio of CdO (Alfa Aesar, 99.998%), CdS (Alfa Aesar, 99.999%), and Nb_2O_5 (Alfa Aesar, 99.998%). $Cd_2Nb_2O_7$ was fired in air at 500 °C for 10 h and 1000 °C for 120 h to prevent the volatilization of Cd. Samples containing S were sealed in evacuated fused silica ampoules and annealed at 1050 °C for 24 h. Synchrotron diffraction studies were per-

formed with a $\lambda = 0.4137810$ Å on the 11BM beam line at the Advanced Photon Source, Argonne National Laboratory. Diffraction data was refined through the Le Bail[43] and Rietveld[44] methods using the GSAS software and EXPGUI user interface.[45,46] Data were fit using profile type 3 for constant wavelength data, and lorentzian size and shape broadening terms were refined. Crystal structures were visualized using the VESTA suite of programs.[47] Transformations from high-symmetry space groups into low symmetry subgroups were performed using the TRANSTRU program on the Bilbao Crystallographic Server.[48–50]Bond Valence Sums (BVS) and Madelung energies were calculated using the EUTAX program.[51]

First Principles Calculations

Calculations were performed using Density Functional Theory (DFT) as implemented in the Vienna Ab initio Simulation Package (VASP)[52,53] using a planewave basis set with a 750 eV energy cutoff. The Perdew-Burke-Ernzerhof (PBE) exchange-correlation functional revised for solids (PBEsol)[54] was used, along with the projector-augmented wave (PAW) method to treat the separation of the core and valence electrons.[55] Low-energy structures used to assess the ground state of $Cd_2Nb_2O_7$ were identified from both experiment and group theoretical methods. These structures were then relaxed fully (ions and lattice degrees of freedom) using primitive cells until the forces and stress tensor were converged to 10^{-3} meV Å^{-1} and 6.2×10^{-3} meV Å^{-2}, respectively. The Brillouin zone was sampled using a $7 \times 7 \times 7$ Monkhorst-Pack and the tetrahedron smearing scheme. Phonon frequencies at the Γ point of the non-primitive cubic structure were found using the frozen-phonon method after relaxing atomic positions with the experimental lattice parameters held constant. Phonon calculations employed a $6 \times 6 \times 6$ Monkhorst-Pack mesh and used the larger conventional cell. Analysis of the distortion modes was informed through the use of the ISODISTORT[56] and AMPLIMODES[57,58] software.

Results

Characterization of the high temperature paraelectric phases

Table 1: Refined crystallographic data for the high temperature, paraelectric phases of the series $Cd_2Nb_2O_{7-x}S_x$. * indicates values associated with additional strain modeling phases (25.5 and 22.0 wt. %, respectively).

Refined formula	$Cd_{1.96(2)}Nb_2O_{6.95(2)}$	$Cd_2Nb_2O_{6.88(1)}S_{0.22(1)}$	$Cd_2Nb_2O_{6.28(1)}S_{0.72(1)}$
Temperature (K)	340	340	440
Space Group	$Fd\bar{3}m$ (#227)	$Fd\bar{3}m$ (#227)	$Fd\bar{3}m$ (#227)
a (Å)	10.37341(1)	10.52151(4)	10.57098 (1)
		*10.51106(4)	
		*10.48658(4)	
Volume a (Å^3)	1116.256(5)	1164.757(5)	1181.260(5)
Z	8	8	8
Formula weight	519.10	526.04	534.16
Cd U_{iso} (Å^2)	0.013(2)	0.039(5)	0.0537 (2)
Nb U_{iso} (Å^2)	0.0078(5)	0.0098 (5)	0.0117(3)
R (%)	9.4	5.8	7.6
R_{wp} (%)	11.2	8.2	9.2

Synchrotron diffraction measurements were carried out above and below the ferroelectric transition temperature, T_c, on samples of $Cd_2Nb_2O_{7-x}S_x$ for nominal values $x = 0$ (T= 340 K, 100 K), 0.25 (T= 340 K, 100 K), and 0.7 (T= 440 K, 100 K). A nominal sample of $Cd_2Nb_2O_6S$ was attempted with the CdS, CdO, and Nb_2O_5 precursors, but the highest phase-pure sample achieved was the nominal $x = 0.7$ sample. The literature synthesis of nominal x=1 was reported by the reaction of CdS and $CdNb_2O_6$,[59] but our attempts did not yield the pyrochlore phase. All compositions index to a cubic space group of $Fd\bar{3}m$ above T_c. The presence of a minor (less than 3%) $CdNb_2O_6$ impurity phase was detected in all compositions and included in the fit. A cadmium deficiency was found in the nominal x=0 sample, accompanied by an oxygen deficiency on the O' site, maintaining charge neutrality of the compound. The Rietveld fits for the samples are presented in Supplemental Figure S1, and a summary of all refined parameters is found in Table 1. Values close to the nominal compositions were obtained for S-substituted compositions.

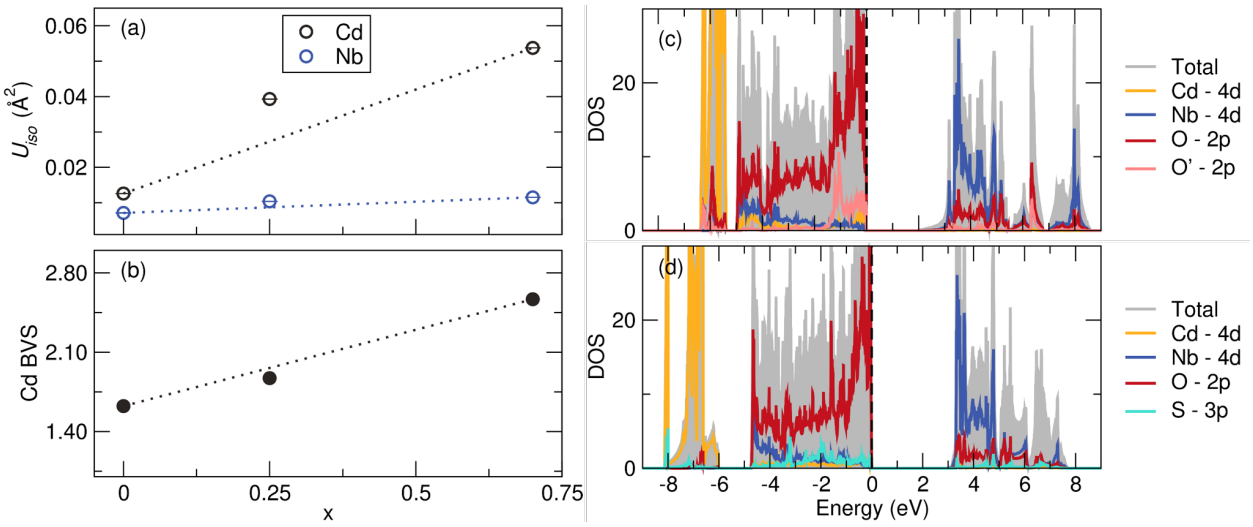

Figure 2: Refined parameters as a function of S content, x for the series $Cd_2Nb_2O_{7-x}S_x$ in the cubic $Fd\bar{3}m$ phase: (a) A general increase in the atomic displacement parameter (ADP), U_{iso}, is observed for both cations with increasing S content, but this trend is much more dramatic in the Cd cation. (b) Calculated bond valence sums (BVS) of the Cd cation illustrate that it is under-bonded in the nominal $x = 0$ sample, and its valency is raised with S substitution. Density of States calculations for (c) $x = 0$ and (d) theoretical $x = 1$ reveal higher covalent bonding on the Cd_2X' sublattice upon sulfur substitution, indicated by broadening of the Cd 4d band and the removal of O' states from the valence band.

An increase in S content was accompanied by an increase in the lattice parameter and Cd-O2/S bond length. Table 1 presents the change in the lattice parameter as a function of S-doping, x. An expansion of the cell edge is anticipated as the larger S is substituted for O, and while this is observed, it does not strictly obey Vegard's Law (Supplemental Figure S2) and deviates from linear behavior. This can be explained by inhomogeneity with respect to the S content in the nominal $x = 0.25$ sample, evident by large tailing in the peaks (Supplemental Figure S3). Such inhomogeneity can often be modeled as strain but was too asymmetric to be modeled by fitting a Lorentzian strain broadening term, and multiple pyrochlore phases were incorporated into the fit in order to accurately model the tailing. The origin of the sample inhomogeneity may be due to a gradient or pockets of S-poor regions throughout the bulk material, indicated by tailing to the low-d sides of the peaks These regions modeled as "different phases" may be a result of the sample attempting to phase-separate, but cooling was too rapid to resolve the various phases. Due to the large

space inside the pyrochlore channels, it was predicted that S substitution would take place on the 8*b* O' site in the pyrochlore lattice. Refinements of S occupancy on the 8*b* site yielded better agreement with the experimental data than occupancy on the 48*f* site, and attempts to place S on the 48*f* site resulted in a refined value of 0.98(2) O occupancy on the site.

Analysis of the atomic displacement parameters (ADP, modeled as U_{iso}) can provide insight into the existence of any local structural disorder present in the samples. ADP values for both the Nb^{5+} and Cd^{2+} cations (Figure 2a) increase with increasing S content, but this effect is much more dramatic on the Cd site in comparison to the Nb site. It must be noted that the $x = 0.7$ sample has been collected at 100 K higher than the rest of the series, and the increased thermal energy is contributing to the elevated ADPs for the $x = 0.7$ sample; analysis of the lower temperature data is needed to further draw conclusions. When modeled anisotropically (U_{ani}) with values converted to root mean square (RMS) displacement values for the *A*-site cation, larger values are found perpendicular to the 3-fold axis than parallel to this axis, as is commonly seen with pyrochlores.[8] For the nominal x=0 samples, RMS values are determined to be 0.14 and 0.08 Å; for x=0.25, 0.20 and 0.19 Å; for x=0.7, 0.25 and 0.2 Å. The higher values for the x= 0.25 and 0.7 are likely due to structural disorder in the form of incoherent atomic positions (and thus incoherent bond distributions between the *A*-site cation and *X*' anion) within the channel structure. The trend of increased structural disorder within the pyrochlore channel is corroborated with the ADPs of the anions with increasing S content. The ADP of the O in the NbO_6 framework of the structure decreases with S substitution, whereas the channel O'/S ADP increases. The combination of the elevated ADPs of the Cd and O'/S with S substitution indicates structural disorder is induced within the pyrochlore channel, and increases with increasing S content.

Calculations of the bond valence sums (BVS) of the Cd^{2+}cation throughout the solid solution (Figure 2b) reveal under-bonded Cd in the nominal $Cd_2Nb_2O_7$, with a BVS of 1.6. This is relieved upon the addition of S, as a steady increase in the BVS of Cd is observed with increasing S-content. This also indicates that the degree of covalency between the Cd

and 8*b* anion is higher when more S is present, which agrees with the expected trend based on the electronegativities and sizes of O and S. The BVS of Nb was calculated (within a range of 4.7–5.2), but does not appear to be systematic based on the S-content, which is expected as S-substitution is exclusively on the Cd-O'/S chain.

Changes in the bonding character are also discernible in the electronic density of states (DOS). Atomic and orbital projections of the DOS were computed for the $x = 0$ and theoretical $x = 1$ relaxed $Fd\bar{3}m$ structures (Figure 2c and d). The replacement of O with S on the Cd_2O' sublattice leads to a narrowing of the O-dominated valence band and a broadening of the Cd 4d band. The S 3p states are located at lower energy than the O 2p states, resulting in a shift in the DOS from near the top of the valence band to lower energy as the Cd hybridizes more strongly with S than with O. In addition, the DOS provides evidence of the connection between the NbO_6 and Cd_2O' sublattices, as under S substitution there is a narrowing of the Nb-dominated conduction band. The replacement of O with S on the Cd_2X' sublattice is associated with a marginal increase in the Nb-O bond length and the lattice parameters (by about 1.5% and 2.7% respectively) which should slightly reduce the strength of the bond between Nb and O. However, we believe that the narrowing of the conduction and valence bands is primarily explained by the removal of O' states from the valence band, as the S 3p orbitals sit at lower energy than the O 2p, altering the hybridization of the X' site.

Characterization of the low temperature ferroelectric phases

A comparison of the high temperature and 100 K data for each nominal sample can be seen in Figure 3. For the (a) $x = 0$ sample, reduction in peak height is evidenced upon cooling, and subtle peak splitting of the (400) cubic can be observed, while in the (b) $x = 0.25$ the (400) cubic peak splits into a doublet. For the (c) $x = 0.7$ sample, no peak splitting is observed; however, new peaks emerge upon cooling around approximately 2.2 $Å^{-1}$ and the (311) cubic peak intensifies. Both peak splitting and new peaks suggest a lowering in symmetry, but the

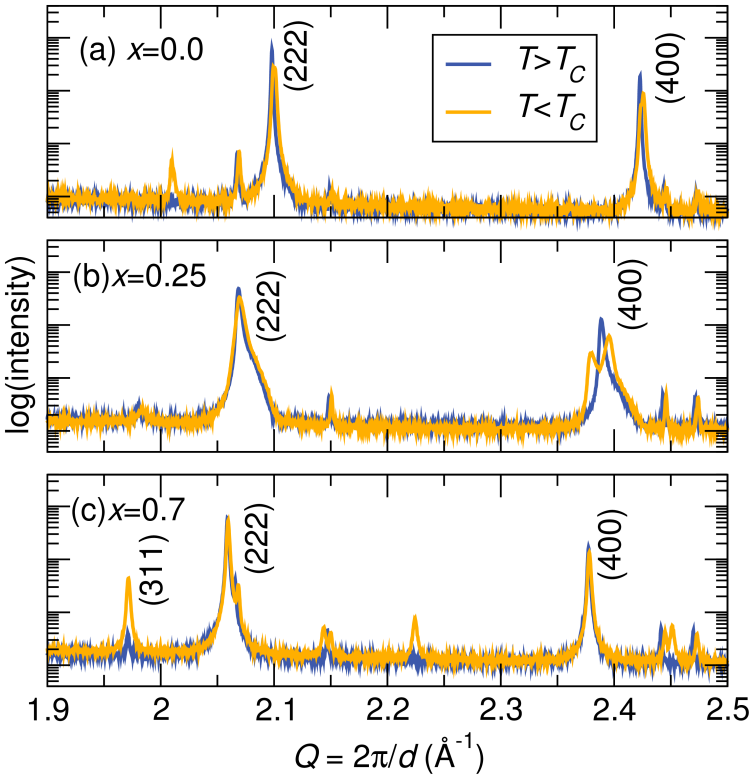

Figure 3: Comparison of the raw X-ray data above ($T > T_C$) and below ($T < T_C$) the ferroelectric transition temperature for the series $Cd_2Nb_2O_{7-x}S_x$. For the (a) $x = 0$ and (b) $x = 0.25$ samples peak splitting is observed, while in the (c) $x = 0.7$ sample new peaks emerge without peak splitting. All (hkl) values are in reference to the high temperature $Fd\bar{3}m$ structure.

lack of peak splitting suggests the $x = 0.7$ sample retains a cubic structure.

Structural Characterization of $Cd_2Nb_2O_7$ at 100 K

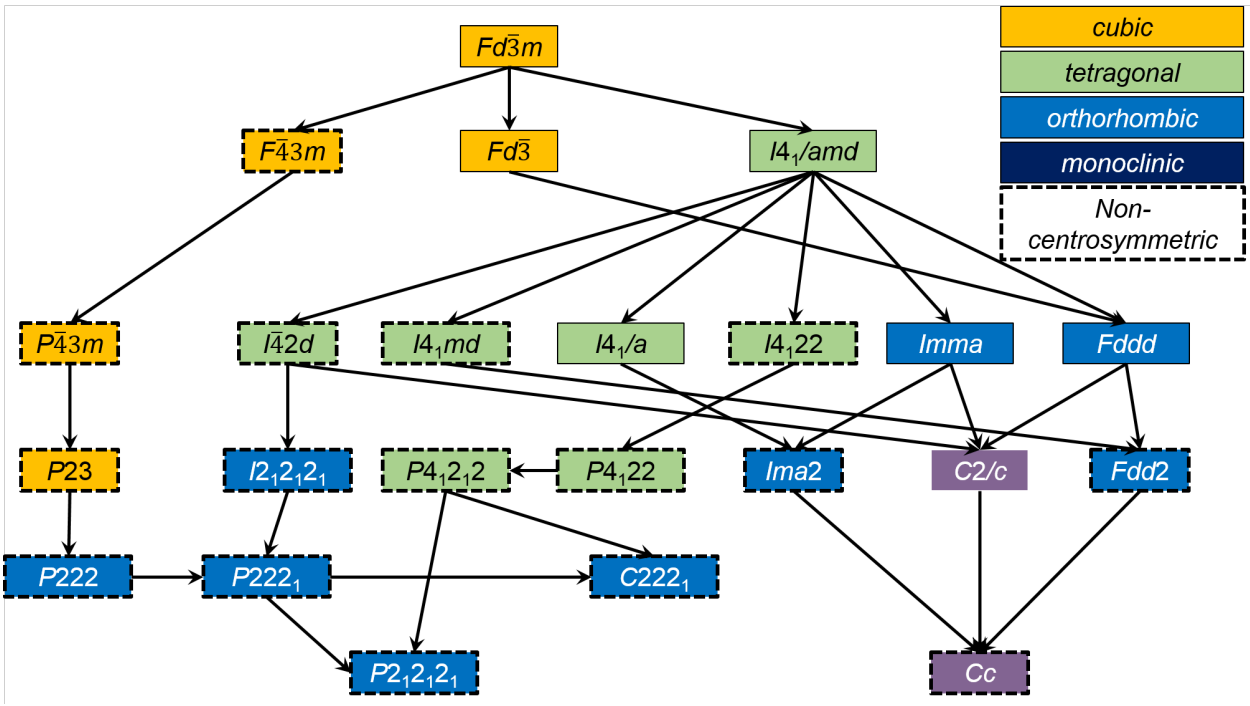

Figure 4: Group-subgroup relationships for the high-symmetry cubic $Fd\bar{3}m$ space group of the high temperature pyrochlore samples. Space groups outlined in a dashed line indicate non-centrosymmetric aristotypes.

To determine the space groups of the low temperature ferroelectric phases, various subgroups of the high temperature $Fd\bar{3}m$ phase (illustrated in Figure 4) were considered. Low temperatures structures have been reported from tetragonal,[31] orthorhombic,[32] and rhombohedral[33] systems, with $Ima2$[31] and $I\bar{4}m2$[40] from powder refinements. As the material has been widely reported as polar through various techniques, the $I\bar{4}m2$ space group was not considered. Orthorhombic models were chosen to model the low temperature structure due to the evidenced peak splitting of the (400) peak, and Rietveld refinement indicated the $Ima2$ space group as the best description of the structure at 100 K. Lattice parameters and bond lengths are in reasonable agreement with the literature.[35,36] Upon cooling, Cd and Nb split from the fixed 16d and 16c Wyckoff positions, respectively, to the variable 4a

and 4*b* sites each. In this new configuration, refinements indicate Cd1 and Cd2 displace by approximately 0.05 Å and 0.10Å from the ideal positions, while Nb1 and Nb2 displace by approximately 0.20 Å and 0.15 Å, respectively.

The Cd_2O' and NbO_6 networks undergo significant distortions in the low temperature structures. At room temperature, the NbO_6 octahedra are uniform, exhibiting only one Nb–O bond. Distortions in the octahedral environments of both Nb1 and Nb2 are observed upon transition to the lower $Ima2$ phase, arising from the propensity towards off-centering in the second-order Jahn-Teller (SOJT) d^0 Nb^{5+} cations.[60–62] In the $Fd\bar{3}m$ phase there is one Cd–O' bond throughout the Cd_2O' network. Upon transitioning into the $Ima2$ structure, there is a correlated displacement of the Cd2 cations along the Cd_2O' chain in the crystallographic [001] direction, resulting in alternating ordered short and long bonds in the Cd–O' chain. Chains of $Cd1_2O$' along the crystallographic [100] direction retain a single Cd–O' bond. Calculations of BVS at room and low temperatures indicates that the average BVS of Cd is slightly raised from 1.62 at room temperature to 1.66 in the low temperature structure, indicating that the alternating short and long Cd2–O' bonds help alleviate the under-bonded nature of Cd. This increase in Cd^{2+} BVS upon cooling suggests the Cd_2O' network as an additional structural instability that drives the transition to the low temperature structure.

To investigate the relationship between the Cd–O' and NbO_6 networks, refinements on the phase transitions in the non-ferroelectric $Cd_2Ta_2O_7$ have been performed, illustrated in Figure 5. Both data sets can be indexed to the $Fd\bar{3}m$ space group, but peak intensity is significantly decreased at low temperatures, indicating structural distortions upon cooling. However, the absence of systematic symmetry lowering (*i. e.* peak splitting or the emergence of new peaks) indicate neither network undergoes correlated distortions at lower temperatures. The absence of correlated distortions may be driven by a lack of correlated SOJT activity in the Ta^{5+} cations, which are heavier *d*-block cations and have lower propensity for off-centering. Sleight and Bierlein[63] studied the $Cd_2Nb_{2-x}Ta_xO_7$ system using second harmonic generation (SHG), differential scanning calorimeter (DSC), and X-ray diffraction

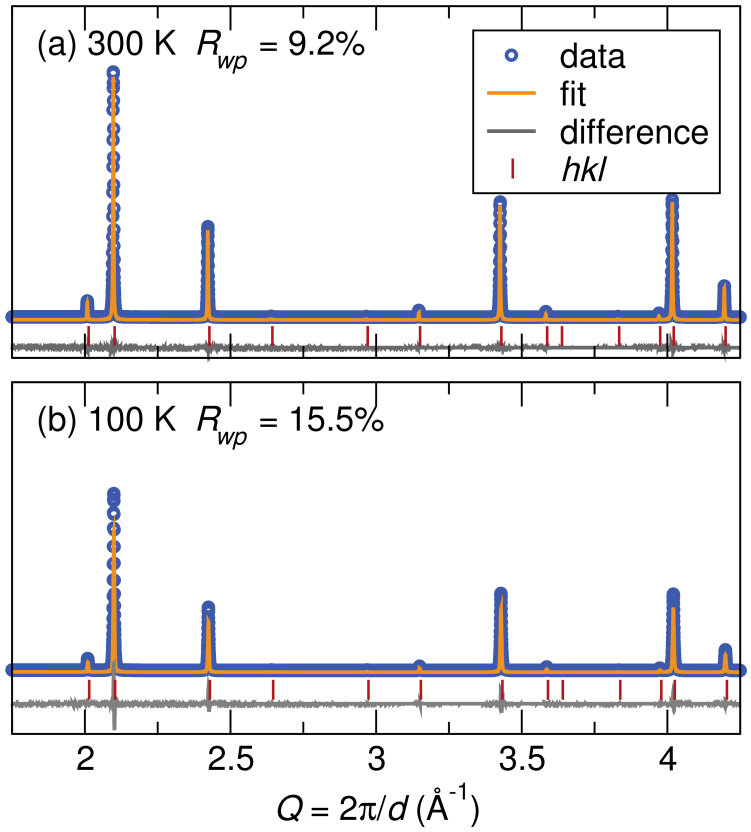

Figure 5: Rietveld fits of synchrotron X-ray data collected on $Cd_2Ta_2O_7$ collected at (a) 300 K and (b) 100 K. Both data sets can be indexed to the $Fd\bar{3}m$ space group, but peak intensity is decreased at low temperatures, indicating structural disorder upon cooling.

(XRD). DSC indicated a phase transition near 200 K for most samples, including $x = 2.0$ ($Cd_2Ta_2O_7$). However, an SHG signal indicating an absence of a center of symmetry was only observed below 200 K for samples containing some Nb, found in $Cd_2Nb_{0.02}Ta_{1.8}O_7$ but not in $Cd_2Ta_2O_7$. The XRD study of $Cd_2Ta_2O_7$ showed a change in peak shape below 200 K, which was interpreted as unresolved peak splitting due to loss of cubic symmetry. Our synchrotron data for $Cd_2Ta_2O_7$ at 100 K show a change in peak shape with increased peak width. This could also be interpreted as unresolved peak splitting.

Additionally, Madelung energies of the Nb and Ta structures were calculated at 100K. For $Cd_2Nb_2O_7$, the 100 K $Ima2$ structure has a calculated energy of -46,366.16 kJ/mol. $Cd_2Ta_2O_7$ retains the $Fd\bar{3}m$ space group at 100 K, and has a calculated energy of -46,408.13 kJ/mol. In these calculations, Nb and Ta are treated the same with a +5 charge. The real charges on Nb and Ta are much less, but it can be assumed that the real charge on Ta is higher than on Nb because the generally accepted electronegativity values are 1.6 for Nb and 1.5 for Ta. This means that the Madelung energy will be of more importance for $Cd_2Ta_2O_7$ than $Cd_2Nb_2O_7$. The repulsive interaction between the M^{5+} cations are evenly spaced in the cubic structure, and therefore will prevent the transition to lower symmetry because the higher symmetry structure has more favorable electrostatic interactions between the higher charged Ta cations. In addition to this Madelung cost, the polarizability of the Nb–O and Ta–O bonds plays a role in the propensity to distort to a lower symmetry structure. The energy of the empty $4d$ orbitals of Nb are close in energy to the filled $2p$ orbitals of O, which leads to facile mixing of the $4d$ and $2p$ orbitals. This allows Nb to easily move away from the center of the octahedron, undergoing a second order Jahn-Teller distortion and resulting in a polar NbO_6 coordination environment. The energies of the $5d$ orbitals of Ta are further from those of the O $2p$, and as such no distortion is observed with Ta, even though the instability driven by a low Cd^{2+} BVS is present for $Cd_2Ta_2O_7$. The lack of an overall displacement in both networks upon complete Ta substitution suggests the displacements of the two networks in $Cd_2Nb_2O_7$ are cooperative, and this understanding can help guide the exploration of novel

ferroelectric pyrochlores.

First principles calculations of $Cd_2Nb_2O_7$

First principles calculations were performed to investigate transition pathways and further assess the assignment of the low-temperature structures. Zone-center phonon frequencies of the high temperature $Fd\bar{3}m$ structure were calculated, returning 6 unstable phonon modes grouped into 2 triply degenerate sets at $2.63i$ THz (T_{1u}) and $1.59i$ THz (T_{2u}). These modes, as well as additional unstable phonons from the zone boundary, are listed in Supplemental Table S1. Our calculated frequencies are consistent with previous work,[35,64] indicating dynamical instability of the cubic phase at low temperature. To ascertain the ground state structure, we constructed initial low symmetry structures based on different linear combinations of the soft modes and polar subgroups of $Fd\bar{3}m$ considered above, and then performed full structural relaxation. Four structures with symmetries $Fdd2$ (#43), $I4_1md$ (#109), Cm (#6), and $Ima2$ were found to all be within 2.5 meV/f.u. (Figure 6), which is within the error of the DFT method employed here; however, $I4_1md$ and $Fdd2$ have been conclusively ruled out by Rietveld refinement (Supplemental Figure S4), while the monoclinic Cm phase may be related to subsequent phase transitions at lower temperature.

FHaving identified $Ima2$ as a feasible low temperature space group, the structural distortion modes which modulate the transition from the cubic $Fd\bar{3}m$ structure were investigated. Γ_4^- and Γ_5^- distortion modes were identified as potential order parameters (Figure 7), both with $Ima2$ symmetry and irreducible representations T_{1u} and T_{2u} respectively. Consistent with experimental observation, neither mode alters the single Cd-O bond in the [100] direction, while the Γ_4^- mode produces the alternating long-short bond structure in the [001] structure. Both modes exhibit Nb off-centering, while the Γ_4^- mode also exhibits significant O displacements. While the two modes lift the same symmetries, only the Γ_4^- mode is ferroelectric since the Γ_5^- mode is polar but does not produce a net dipole.

Relaxing the two modes separately results in two different $Ima2$ structures, one matching

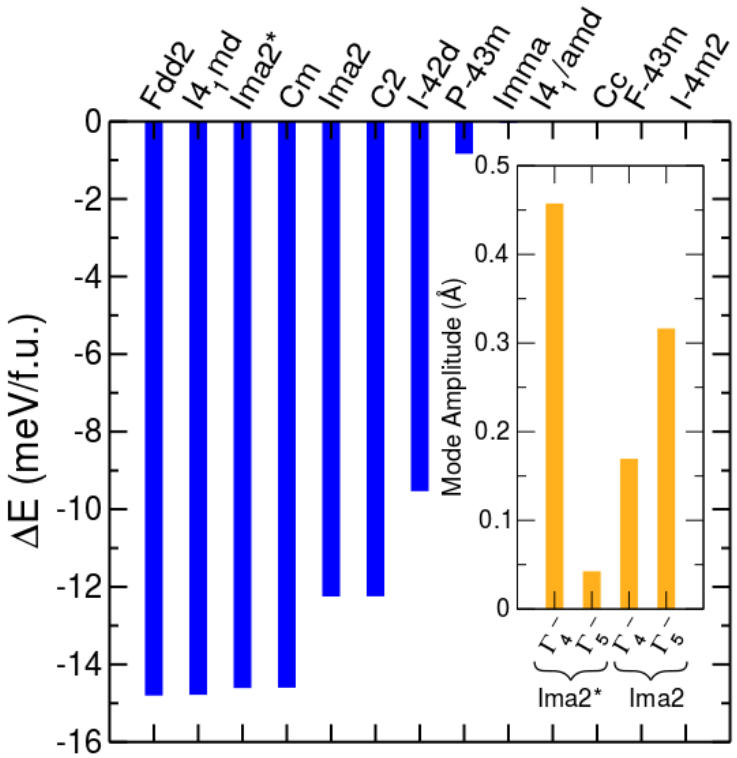

Figure 6: First principles energy per-atom comparison of $Cd_2Nb_2O_7$ in various subgroups of $Fd\bar{3}m$. The $Ima2^*$ structure is found by relaxing the Γ_4^- mode, which differs from the experimental $Ima2$ structure in relative amplitude of the Γ_4^- and Γ_5^- distortion modes (inset).

the experimental $Ima2$ structure (initialized with the Γ_5^- mode) and a new structure (initialized with the Γ_4^- mode) referred to as $Ima2^*$. The Γ_4^- and Γ_5^- modes are both present in both relaxed structures, but in different relative amplitudes (Figure 6 inset). This implies that one of the subsequent structural transitions undergone by $Cd_2Nb_2O_7$ at lower temperatures could be isostructural.

Figure 8 shows the change in energy as the $Fd\bar{3}m$ structure is modulated by distortion patterns associated with various phonon modes. These phonon modes are the softest modes to exhibit the irreducible representations found in the symmetry adapted mode decomposition. $T_{1u}(1)$ ($2.63i$ THz) shares the same irreducible representation as the Γ_4^- symmetry-adapted mode and lowers the energy, but leads to a monoclinic symmetry incompatible with the symmetries lost at the transition into the $Ima2$ structure. Instead, it seems likely that this mode may play a role in the subsequent phase transitions to the proposed monoclinic phases.[35–37] Our analysis shows that $T_{2u}(1)$ ($1.59i$ THz), on the other hand, fulfills 98.7% of the distortion present in the Γ_5^- symmetry-adapted mode, breaking the symmetries necessary to give the $Ima2$ space group and sharing the same T_{2u} irreducible representation. For that reason, we propose that the T_{2u} mode drives the $Fd\bar{3}m \rightarrow Ima2$ phase transition, with the other modes condensing as a result of instabilities produced by this primarily Nb off-centering distortion.

Structural characterization of S-substituted samples at 100 K

Rietveld fits of the $x = 0.25$ at 340 K indicate the material can be described by the cubic $Fd\bar{3}m$ structure with significant lattice strain. Upon cooling, this strain, evidenced by asymmetric peak tailing, is still apparent in the cubic (222) peak, but the (400) and related peaks split. This peak splitting upon cooling of (l00) peaks indicates a lowering of symmetry from the cubic high temperature structure. Le Bail fits were first performed against candidate orthorhombic subgroups of $Fd\bar{3}m$, $I4_1/amd$ and $I4_1md$, but these space groups were unable to index all peaks in the diffraction pattern (Supplemental Figure S5). Symmetry was

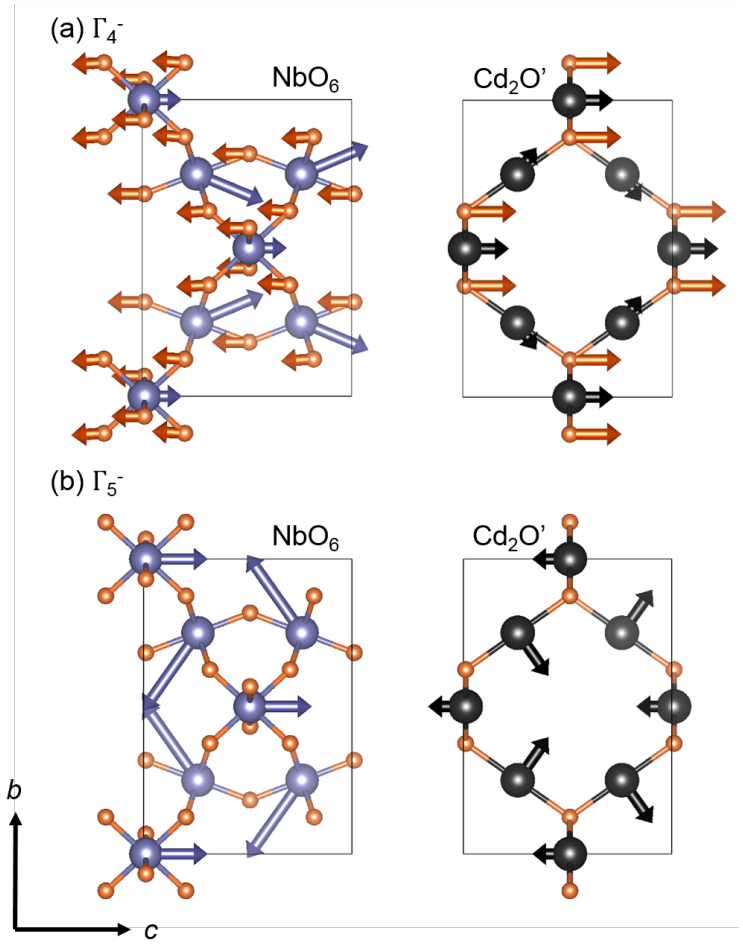

Figure 7: Illustration of the (a) T_{1u} and (b) T_{2u} mode distortions which characterize the crystal structure at 100K for the parent oxide sample. The T_{1u} distortion produces correlated displacements in both networks, resulting in a net dipole. The T_{2u} is also polar, but involves no net displacement of charge and thus is not FE active.

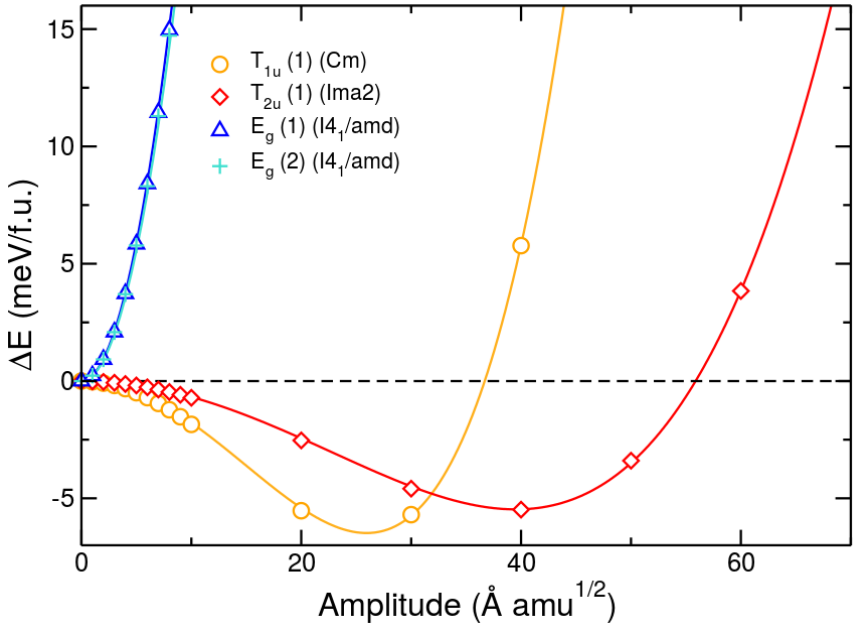

Figure 8: Energy evolution as the T_{1u}, T_{2u}, and E_g phonon modes amplitudes are modulated. Both the T_{1u} and T_{2u} distortions lower the energy, although only the T_{2u} mode exhibits symmetry compatible with the low temperature $Ima2$ structure. Lines are a 4th degree polynomial fit to the data, and the mode amplitude is given in units of angstroms times the square root of the atomic mass unit (amu).

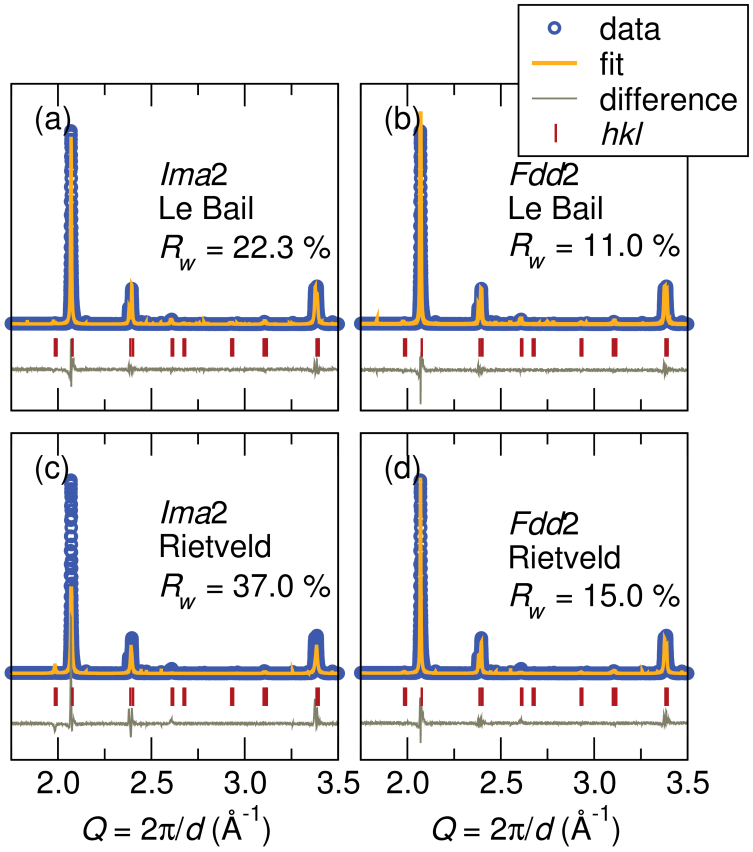

Figure 9: Fits of the 100 K data for the nominal $x = 0.25$ sample: Le Bail fits against the orthorhombic space groups (a) $Ima2$ and (b) $Fdd2$ indicates all peaks can be indexed by both space groups, while Rietveld fits suggest (d) $Fdd2$ is a better candidate than the (c) $Ima2$ structure.

further lowered and Le Bail fits were performed against orthorhombic subgroups $Ima2$ and $Fdd2$ (Figure 9a and b), both of which were able to index the peak splitting observed at 100 K. To further differentiate between the two space groups, Rietveld refinements were performed (Figure 9c and d), and the $Fdd2$ structure yielded a significantly better fit than $Ima2$ adopted by the full oxide parent compound. As with the 340 K data, the asymmetric peak tailing was modeled with several $Fdd2$ "strain" phases, reported in Table 2.

The resulting $Fdd2$ structure is illustrated in Figure 10a, shown as the single phase with no strain simulation phases. Distortions in the NbO_6 network indicate local distortions of the Nb towards the face of the octahedra, resulting in a cooperative distortion of the Nb cations along the crystallographic [001] direction. Distortions of the Cd–O'/S network illustrate that all Cd cations are displaced towards one O'/S, resulting in alternating long and short Cd–O'/S bonds along a single chain. In the crystallographic structure, these distortions are such that all Cd cations are displaced globally along the [001] direction. A combination of the two interpenetrating networks reveals that both networks are cooperatively displacing along the [001], suggesting these networks are coupled more strongly than in the oxide parent compound. This could be a result of the increased covalency of the Cd–S interactions, as observed on the BO_6 network when B= Nb instead of Ta.[63]

Higher substitution of S into the pyrochlore further alters the observed structure at 100 K. At a nominal value of $x = 0.7$, the lack of peak splitting in XRD patterns suggests that cubic symmetry is retained. However, additional peaks appear that violate face centering. By lowering the symmetry into the $P\bar{4}3m$ (#215) space group, all peaks are indexed. Rietveld analysis indicates the intensity of certain peaks is poorly described in this model, particularly the (321) and (420) peaks (Supplemental Figure S6c and Table S3). ADPs of the atoms in the NbO_6 network are reasonably small, indicating these sites are well described. With this model, there appears to be a large amount of positional disorder in the Cd–O'/S network, evidenced by site disorder of O'/S and enlarged, anisotropic ADPs of the Cd1 site. Upon lowering the symmetry to $P\bar{4}3m$, the 8b position is split into two crystallographic sites, and

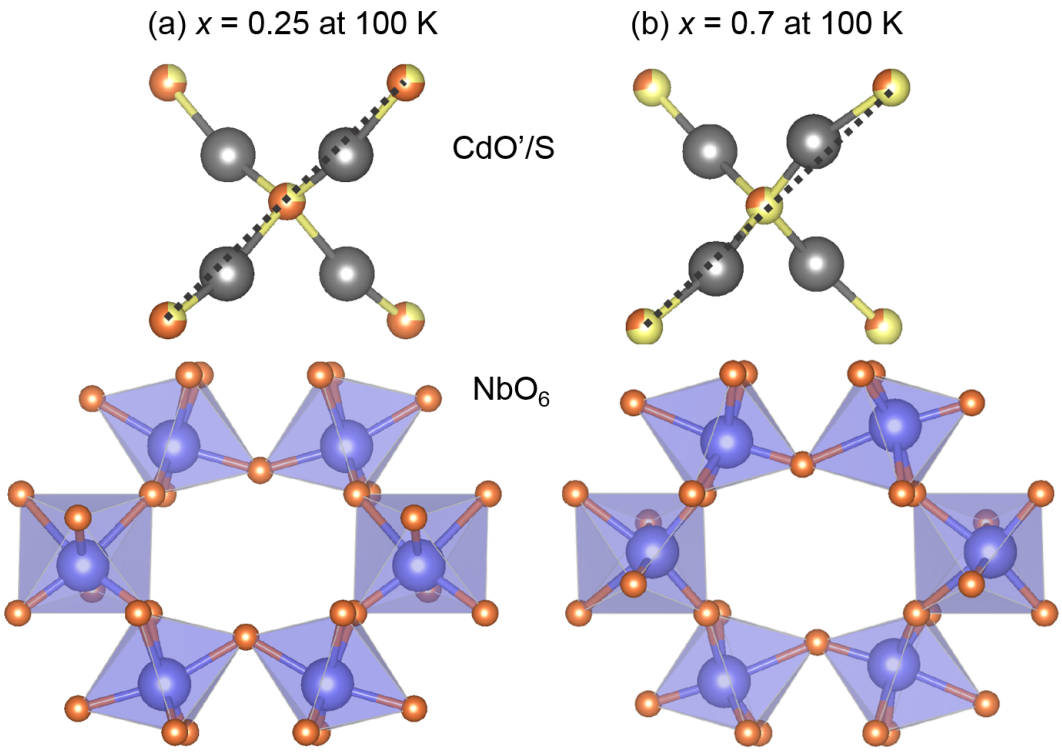

Figure 10: Refined Rietveld structures of the (a) x = 0.25 with space group $Fdd2$ and the (b) = 0.7 with space group $P2_12_12_1$ at 100 K illustrate the differences in the two pyrochlore networks with varying sulfur content.

a slightly better fit is obtained when the O' and S are shared on only the $3c$ site at $(0, \frac{1}{2}, \frac{1}{2})$ rather than distributed across the three crystallographic sites (R_{wp} = 22.4 % and 22.6 % respectively). The literature surrounding the solid solutions between pyrochlore oxides and sulfides is sparse,[59,65] presumably arising from the drastic size difference between O and S (1.40 vs 1.84 Å, respectively).[66] In the case of the pyrochlores, this substitution is tolerated due to the great flexibility of the A_2X' network with X'-A-X' linkage that can easily bend. The $P\bar{4}3m$ structure provides a reasonable description of the NbO_6 network, indicated by small U_{iso} values on the Nb sites, but the description of the Cd_2X' network with this model remains a challenge to describe.

Early work on reported $Cd_2Nb_2O_6S$ suggests a tetragonal structure for the β and γ phases,[65] and speculated that when $x = 1$, the S-Cd-S angle is no longer 180°,[59] resulting in a loss of 3-fold rotation axes on the Cd_2X' network. In the $P\bar{4}3m$ model, this is true for the majority of the network; however, 25 % of Cd remain on a 3-fold axis. Therefore, the apparent positional disorder in the network as described by the $P\bar{4}3m$ structure may be captured by lowering the symmetry to a space group that removes all 3-fold symmetry from the Cd-X' network. The size mismatch between the Cd_2X' network and the NbO_6 network changes drastically as S substitutes for O on the X' site. The Cd_2O' network is somewhat stretched in $Cd_2Nb_2O_7$, as indicated by the BVS of Cd and O'. The ideal A_2X' network would become much larger with added S, much too large to be accommodated by the NbO_6 network. The ideal Cd_2X' network would be under extreme pressure if it did not distort. A solution to this mismatch was sought by analogy to the cristobalite form of SiO_2, which has the pyrochlore A_2X' structure with cations and anions interchanged. On cooling from high temperature the space group changes from $Fd\bar{3}m$ to $P4_12_12$ (#92) with a 5% volume decrease in the unit cell. In this $P4_12_12$ model all Cd-X'-Cd angles deviate from 180°. The formula unit, Z, is 4 for the tetragonal structure and 8 for the cubic structure; however, Z is 2 for the primitive version of the face centered cubic cell. Therefore, by lowering symmetry to the tetragonal structure would generate the peaks violating face centering that emerge

upon cooling in $Cd_2Nb_2O_6O'_{0.3}S_{0.7}$.

Initial refinements in the $P4_12_12$ (#19) cristobalite structure indicate a better description of the structure than the $P\bar{4}3m$ model, resulting in a R_{wp} value of approximately 16 % (Supplemental Figure S6d and Table S3). The cristobalite model yields reasonable bond distances for the Cd-X' network (approximately 2.29 and 2.32 Å); however, nonphysical negative U_{iso} values for the X' sites were found upon refinement, and were therefore fixed to a value of 0.01 Å^2. The drop from cubic to tetragonal is supported by the refined lattice parameters of $a = b = 7.4737(7)$ and $c = 10.5670(2)$ Å (where the unrefined transformed cell from cubic symmetry has cell edges of $a = b = 7.4720$ and $c = 10.5670$ Å), indicating the unit cell has a slight tetragonal distortion which improves the overall fit. Additionally, this refined tetragonal distortion is supported by metrically comparing the square root of 2 multiplied by the refined a lattice parameter, which yields a value of 10.5693(2). This is significantly different from the refined c lattice parameter (by 0.0024 Å, which is approximately 10 times the standard deviation of the refined values), supporting the drop from cubic to tetragonal symmetry.

Although the structure is evidently improved through the cristobalite model, there are still features that cannot be completely described by this model, as evidenced by the negative ADPs of the X' anions. In the cristobalite structure, all Cd occupy the same crystallographic site, and therefore all X'Cd_4 tetrahedra are forced to be the same. Given the large size and electronegativity differences between the two X' anions on the 8b site, is it reasonable to expect various bond lengths will be preferred between Cd–S' and Cd–O'. Therefore, a model that allows for a mixture of O'Cd_4 and S'Cd_4 tetrahedra with short and long bonds, respectively, was considered to further improve the structural description. Lowering the space group to $P2_12_12_1$ splits the cation sites from one to two distinct crystallographic positions, allowing for crystallographically different X' coordination environments.

The refined $P2_12_12_1$ structure demonstrates an improvement over the cristobalite model, illustrated in Supplemental Figure S6e and Table S3. While one Cd site has a rather large

U_{iso} value (0.04 Å^2), the second site has a much lower U_{iso} value of 0.002 Å^2, relieving the apparent structural disorder as observed in higher-symmetry models. Moreover, all parameters were able to be refined to yield physical values, including the X' site. In the $P2_12_12_1$ structure, the X'-Cd-X' bond angle deviates from the cubic 180° by about 15°, illustrated in Figure 10. This is accompanied by a change in the coordination number of Cd from 2 to 4, and an increase in the coordination numbers of the three nearby O of the NbO_6 network (O3 and O6 increase from a CN of 2 to a CN of 3, and O4 increases from a CN of 2 to a CN of 4)NSLS-II. The distortion of the the Cd_2X' network is so strong that some Cd–O distances have become essentially as short as the Cd–X distances, as also occurs in $Bi_2Sn_2O_7$,[67,68] the only other reported pyrochlore where a similar distortion is present.

The bonding of Cd to O of the NbO_6 network is significant and is therefore expected to impact Nb–O distances. The BVS values for Nb are favorable (5.1 and 5.2 for the two sites) evidencing that the variation of Nb–O bond lengths is tolerated due to the polarizability of the Nb d^0 cation, and is likely caused by the Cd bonding to O of the NbO_6 network. In addition to distortions of the B-site cation, distortions due to the electron configuration of the Cd^{2+} may also be contributing to this ability to distort. The d^{10} distortion (2-fold linear) found in oxides for Cu^{1+}, Ag^{1+}, Hg^{2+}, etc. is generally thought to be the reason why $Cd_2M_2O_7$ pyrochlores form so readily.[69] This d^{10} distortion is much less prevalent for sulfides than oxides. Tetrahedral coordination for O is highly favored for oxides where its CN is 4 due to the propensity for sp^3 hybridization. The increased separation between the s-p levels as the principle quantum number increases with S, Se , and Te make sp^3 hybridization unfavorable and less likely to require tetrahedral coordination with $M-X-M$ bonds close to 109.5°. Therefore, it is proposed the O-Cd-O linkage resists bending away from 180° due to the d^{10} configuration and sp^3 hybridization of O, while the S-Cd-S linkage is less prone to stabilize this configuration, and thus does not resist bending. The BVS values for Cd and X' are high (approximately 2.6-2.8) with S and low with O (approximately 1.4-1.5), which is expected due to the increasing covalency when bonded with S. While the R_{wp} value

of 15.8 % is not significantly lower than the $P4_12_12$ cristobalite model, this ability to refine physical U_{iso} values while simultaneously satisfying valency suggests the $P2_12_12_1$ is a better structural model.

An additional model with space group $C222_1$ (#20) was evaluated for possible ordering of O' and S (see supplemental Figure S6f and Table S3). Ordering was attempted on both sites, in addition to a completely site disordered model. All models resulted in an R_{wp} of about 17.4 %. However, any site with shared S'/O' occupancies yielded unphysical negative values, as well as the second Nb site. Therefore, the $P2_12_12_1$ structure is considered as a reasonable crystallographic description of the Cd-X' network, but the evident high degree of structural disorder induced with high S substitution prompts the study of these materials through local techniques.

Table 2: Refined crystallographic data for the low temperature phases of the series $Cd_2Nb_2O_{7-x}S_x$. * indicates values associated with additional strain modeling phases. An R_{wp}' value, calculated by (R_{wp}/R_{wp} Le Bail), is presented to evaluate the fit of the model beyond limitations of fitting the profile in Le Bail analysis.

Refined formula	$Cd_{1.94(2)}Nb_2O_{6.5(1)}$	$Cd_2Nb_2O_{6.88(1)}S_{0.22(1)}$	$Cd_2Nb_2O_{6.28(1)}S_{0.72(1)}$
Temperature (K)	100	100	100
Space Group	$Ima2$ (#46)	$Fdd2$ (#43)	$P2_12_12_1$ (#19)
a (Å)	7.32066(3)	10.4905(7)	7.4737(2)
		*10.4773	
		*10.4662	
b (Å)	10.37038(6)	10.5603(5)	7.4738(9)
		*10.5455	
		*10.5320	
c (Å)	7.33049(5)	10.5016(7)	10.5669(2)
		*10.4882	
		*10.4776	
Volume a (Å^3)	556.517(5)	1163.36(6)	590.232(5)
Cd1 U_{iso} (Å^2)	0.0058(7)	0.0054(1)	0.041(4)
Cd2 U_{iso} (Å^2)	0.0051(7)	–	0.0024(6)
Nb1 U_{iso} (Å^2)	0.002(8)	0.0128(1)	0.012(3)
Nb2 U_{iso} (Å^2)	0.0014(9)	–	0.0034(9)
R (%)	10.6	13.7	12.0
R_{wp} Le Bail (%)	11.4	11.0	11.7
R_{wp} Rietveld (%)	11.6	15.0	15.3
R_{wp}' (R_{wp} Rietveld/R_{wp} Le Bail)	1.02	1.36	1.31

Discussion

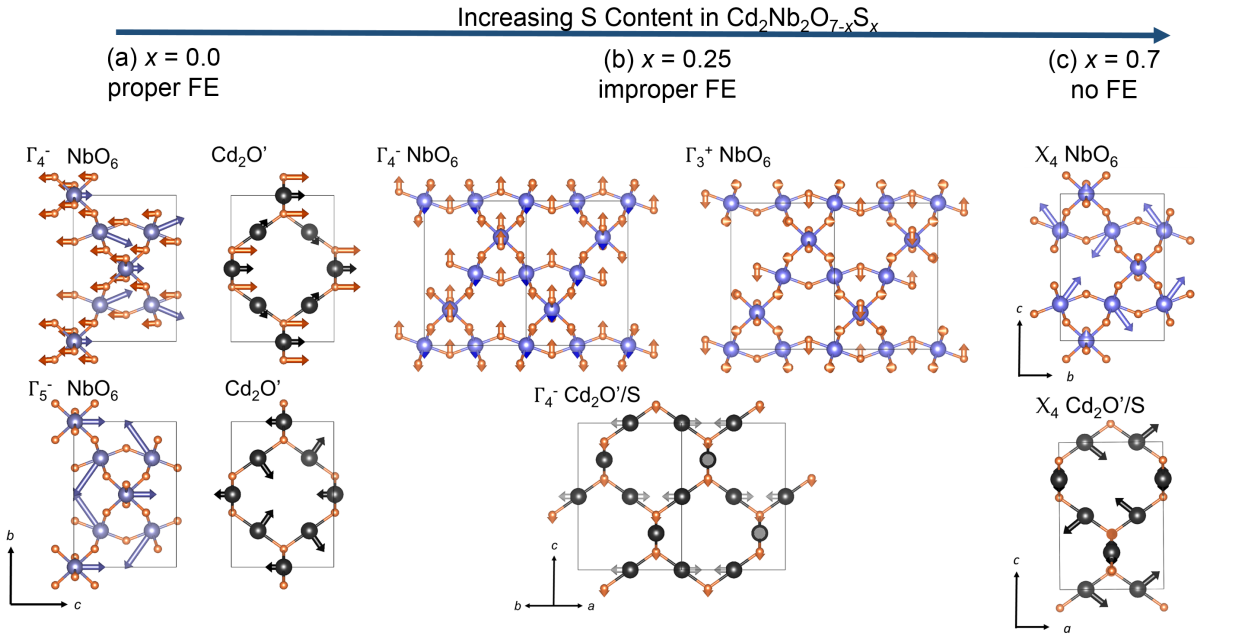

Figure 11: Comparison of the distortion modes of the solid solution reveals that sulfur substitution not only alters the observed low temperature structure, but additionally changes the nature of the phase transition from (a) proper ferroelectric (FE) in the $x = 0.0$ sample, (b) to improper ferroelectric in the $x = 0.25$ sample, to (c) proper noncentrosymmetric (not ferroelectric) in the $x = 0.7$ sample.

Analysis of the experimentally determined high and low symmetry structures at each level of S substitution indicates a change in the nature of the phase transition as S replaces O on the Cd_2O' sublattice. Although it is likely that the transition is best described as a combination of order-disorder and displacive character, we find that the symmetry changes can be accurately modeled using soft mode theory. For $x = 0$, the symmetry of the high and low temperature structures allows for a single mode to lift inversion symmetry. Our study of the lattice dynamics (Figure 8) and distortion patterns corroborates this conclusion, showing that the T_{2u} mode drives the distortion. In addition, the transition from $Fd\bar{3}m$ to $Ima2$ is associated with an increase in the band gap (Supplementary Figure S7), a signature of SOJT-driven proper FE transitions.[70] We know that activation of this mode results in further instabilities which lower the energy, because the $Ima2$ experimental structure sits

about 3meV/f.u. below the energy minima in Figure 8. The energy scale of these interactions may contribute to the reported complex phase transitions which occur between 204 K and 190 K.[26,29,32]

The substitution of S into the pyrochlore channel has severe consequences on the observed structural distortions a lower temperatures. Due to the relatively large space formed by the polarizable NbO_6 network, the *X*'-*A*-*X*' angle easily bends away from 180° to accommodate both O-Cd-O and and O-Cd-S linkages at low x (0.25) and O-Cd-S and S-Cd-S linkages at high x (0.7). Presumably at $x = 0.5$, all 3 linkages would exist with a disordered bond distribution. Our results indicate bending of the *X*'-*A*-*X*' angle away from 180° always occurs with S substitution and is more extreme than has been previously observed for the pyrochlore structure. A similar cristobalite-based structure has been proposed for $Bi_2Sn_2O_7$, with O'-Bi'-O' bond angles ranging between 161.8° and 173.3°.[68] Our results indicate bending of the X'-A-X' angle away from 180° always occurs with S substitution and is more extreme than has been previously observed for the pyrochlore structure without the driving force of a lone-pair bearing cation on the *A*-site.

These large, S-induced distortions may also explain why attempts to substitute S into other systems, such as $Cd_2Ta_2O_7$,[65] have only been reported with small substitution values. When S substitutes into $Cd_2Nb_2O_7$, there is a strong Cd displacement that leads to significant bonding of Cd to a 48*f* O of the NbO_6 network. This must then weaken the corresponding Nb–O bond, resulting in a longer bond length. The high polarizability of the Nb-O bond easily accepts this distortion of NbO_6 octahedron. However, environments less prone to distortions, such as a TaO_6 octahedron, will not be able to accommodate a strong displacement of the *A*-site cation while retaining the valency of the *B*-site cation, making the substitution of S highly unfavorable. Recent synthesis of the the pyrochlore series $Sn_2Nb_2O_{7-x}S_x$ corroborates this with substitution up to $x = 0.6$,[11] proposed to be facilitated by the polarizability of the NbO_6 octahedron.

In addition to drastically altering the observed low temperature structures, the introduc-

tion of S into the Cd_2O' sublattice appears to fundamentally alter the nature of the phase transition. In the $x = 0.25$ sample, although we have not computed the frequencies or energetics of the distorting phonon modes, analysis of the high and low symmetry structures reveals that there exists no group-subgroup relationship. The modes condensed in the low symmetry structure suggest an improper mechanism driven by coupling between Γ_4^- and either Γ_3^+ or Γ_5^- modes (See Supplementary Information Table 2), since either combination of modes would produce $Fdd2$ symmetry. Further increasing the S content leads to yet another change in the phase transition, as demonstrated by the symmetry of the high and low temperature structures in the $x = 0.7$ case. Only the X_4 mode is required to produce the non-polar non-centrosymmetric $P2_12_12_1$ structure.

As a function of S doping the $Cd_2Nb_2O_{7-x}S_x$ series goes from exhibiting a proper FE transition ($x = 0$) to an improper FE transition ($x = 0.25$), followed by a return to a proper noncentrosymmetric transition ($x = 0.7$), the latter being nonpolar but piezoelectric due to the lack of an inversion center. Changes in the dielectric response (see Supplementary Information Figure S8) under S substitution corroborate this description of the $x = 0$ and $x = 0.25$ phase transitions as proper and improper respectively. This result presents a possible pathway towards tuning FE properties of pyrochlore FEs via anion substitution, as the change in phase transition may be used to modulate the susceptibility.

Conclusions

Through the application of high resolution synchrotron data and first principles calculations, a series of phase transitions has been observed in the pyrochlore solid solution $Cd_2Nb_2O_{7-x}S_x$. Distortions in the parent oxide compound indicate the two networks are interrelated, as only the Nb cation has an electronic instability (d^0 electronic configuration) which would lead to off-centering, but displacements are observed in both cation networks. This is corroborated by the lack of a structural transition in $Cd_2Ta_2O_7$, and is attributed to a lower propensity to

off-centering as a result of the less covalent Ta–O bonds. This structural solution confirms the $Ima2$ space group as the 100 K structure, providing insight into the body of work surrounding the $Cd_2Nb_2O_7$ composition.

Sulfur substitution further highlights the interplay between these two networks, as the structural distortion and nature of the phase transition is altered by substitution of the softer anion into the channel of the pyrochlore structure. This is proposed to arise from the increased covalency of the Cd–O'/S network, which may help enhance the off-centering of the Nb cation in the octahedral network. Analysis herein suggests an alternate route for the tuning of polar materials through anion substitution, and illustrates the complex behavior of the interpenetrating pyrochlore networks.

Acknowledgement

Acknowledgment is made to Donors of the ACS PRF (RM), NSF CAREER Award 1541230 (RM), NSF DMR-1508527 (JL and MAS), NSF DMR-1904980 (GL) and Bates College internal funding (SH and GL) for support of this research. GL would like to further thank Prof. Ram Seshadri for many fruitful discussions. Use of the Advanced Photon Source at Argonne National Laboratory was supported by the U. S. Department of Energy, Office of Science, Office of Basic Energy Sciences, under Contract No. DE-AC02-06CH11357. D.H.-Y. acknowledges the Army Research Office (ARO) under Grant No. W911NF-15-1-0017 for financial support and the Department of Defense - High Performance Computing Modernization Program (DOD-HPCMP) for computational resources. J.M.R. was supported by NSF DMR-1454688.

Supporting Information Available

Table of phonon modes and symmetries for $Cd_2Nb_2O_7$. Table of distortion mode decomposition for the series $Cd_2Nb_2O_{7-x}S_x$. Rietveld fits of the 300 K data. Le Bail fits of the

100 K data against various space groups. Electronic density of states for the $Fd\bar{3}m$ and $Ima2$ structures of $Cd_2Nb_2O_7$. Experimental permittivity data. Crystallographic Information Files (CIF) for the high and low temperature structures of nominal $Cd_2Nb_2O_7$, $Cd_2Nb_2O_{6.75}S_{0.25}$, and $Cd_2Nb_2O_{6.3}S_{0.7}$.

References

(1) Cook, W. R.; Jaffe, H. Ferroelectricity in Oxides of Fluorite Structure. *Physical Review* **1953**, *89*, 1297–1298.

(2) Bernard, D.; Lucas, J.; Rivoallan, L. Les Pyrochlores Ferroelectriques Derives de $Cd_2Nb_2O_6S$: Mise en Evidence des Transistions de Phase par des Techniques D'optique Non Lineare. *Solid State Communications* **1976**, *18*, 927–930.

(3) Dong, X. W.; Wang, K. F.; Luo, S. J.; Wan, J. G.; Liu, J. M. Coexistence of Magnetic and Ferroelectric Behaviors of Pyrochlore $Ho_2Ti_2O_7$. *Journal of Applied Physics* **2009**, *106*, 104101.

(4) Liu, D.; Lin, L.; Liu, M. F.; Yan, Z. B.; Dong, S.; Liu, J.-M. Multiferroicity in Spin Ice $Ho_2Ti_2O_7$: An Investigation on Single Crystals. *Journal of Applied Physics* **2013**, *113*, 17D901.

(5) Saitzek, S.; Shao, Z.; Bayart, A.; Ferri, A.; Huvé, M.; Roussel, P.; Desfeux, R. Ferroelectricity in $La_2Zr_2O_7$ Thin Films with a Frustrated Pyrochlore-Type Structure. *Journal of Materials Chemistry C* **2014**, *2*, 4037.

(6) Kimura, M.; Nanamatsu, S.; Kawamura, T.; Matsushita, S. Ferroelectric, Electro-optic and Piezoelectric Properties of $Nd_2Ti_2O_7$ Single Crystal. *Japanese Journal of Applied Physics* **1974**, *13*, 1473–1474.

(7) McQueen, T. M.; West, D. V.; Muegge, B.; Huang, Q.; Noble, K.; Zandbergen, H. W.;

Cava, R. J. Frustrated Ferroelectricity in Niobate Pyrochlores. *Journal of Physics Condensed Matter* **2008**, *20*, 235210.

(8) Sleight, A. W. New Ternary Oxides of Mercury with the Pyrochlore Structure. *Inorganic Chemistry* **1968**, *7*, 1704–1708.

(9) Subramanian, M. A.; Aravamudan, G.; Subba Rao, G. V. Oxide Pyrochlores – A Review. *Progress in Solid State Chemistry* **1983**, *15*, 55–143.

(10) Oka, K.; Hojo, H.; Azuma, M.; Oh-ishi, K. Temperature-Independent, Large Dielectric Constant Induced by Vacancy and Partial Anion Order in the Oxyfluoride Pyrochlore $Pb_2Ti_2O_{2-\delta}F_{2\delta}$. *Chemistry of Materials* **2016**, *28*, 5554–5559.

(11) Giampaoli, G.; Li, J.; Hermann, R. P.; Stalick, J. K.; Subramanian, M. A. Tuning Color through Sulfur and Fluorine Substitutions in the Defect Tin(II, IV) Niobate Pyrochlores. *Solid State Sciences* **2018**, *81*, 32–42.

(12) Kim, J.-K., S.-C. Kang; Kim, S. Synthesis and Characterization of New Pyrochlore-type Oxyfluorides, APbNb$_2$O$_6$F (A = Na and K). *Bulletin of the Korean Chemical Society* **2010**, *31*, 497–499.

(13) Galven, C.; Legein, C.; Body, M.; Fourquet, J.-L.; Buzare, J.-Y.; Le Berre, F.; Crosnier-Lopez, M.-P. New Oxyfluoride Pyrochlores $Li_{2-x}La_{(1+x)/3(2x-1)/3}B_2O_6F$ (B = Nb, Ta): Average and Local Structure Characterization by XRD, TEM and ^{19}F SolidState NMR Spectroscopy. *European Journal of Inorganic Chemistry* **2010**, *2010*, 5272–5283.

(14) Kennedy, B. J. Structural Trends in Bi Containing Pyrochlores: The Structure of $Bi_2Rh_2O_{7-\delta}$. *Materials Research Bulletin* **1997**, *32*, 479–483.

(15) Kennedy, B. J. Oxygen Vacancies in Pyrochlore Oxides: Powder Neutron Diffraction Study of $Pb_2Ir_2O_{6.5}$ and $Bi_2Ir_2O_{7-2y}$. *Journal of Solid State Chemistry* **1996**, *123*, 14–20.

(16) Babu, G. S.; Valant, M.; Page, K.; Llobet, A.; Kolodiazhnyi, T.; Axelsson, A. New $(Bi_{1.88}Fe_{0.12})(Fe_{1.42}Te_{0.58})O_{6.87}$ Pyrochlore with Spin-Glass Transition. *Chemistry of Materials* **2011**, *23*, 2619–2625.

(17) Laurita, G.; Page, K.; Sleight, A. W.; Subramanian, M. A. Investigation of the Anion-Deficient Pyrochlore $AgSbO_3$ through Total Scattering Techniques. *Inorganic Chemistry* **2013**, *52*, 11530.

(18) Shamblin, J.; Feygenson, M.; Neuefeind, J.; Tracy, C. L.; Zhang, F.; Finkeldei, S.; Bosbach, D.; Zhou, H.; Ewing, R. C.; Lang, M. Probing disorder in isometric pyrochlore and related complex oxides. *Nature Materials* **2018**, *15*, 507–511.

(19) Jacob Shamblin, J.; Tracy, C. L.; Palomares, R. I.; O'Quinn, E. C.; Ewing, R. C.; Neuefeind, J.; Feygenson, M.; Behrens, J.; Trautmann, C.; Lang, M. Similar local order in disordered fluorite and aperiodic pyrochlore structures. *Acta Materialia* **2018**, *144*, 60–67.

(20) Vanderah, T. A.; Levin, I.; Lufaso, M. W. An Unexpected Crystal-Chemical Principle for the Pyrochlore Structure. *European Journal of Inorganic Chemistry* **2005**, *2005*, 2895–2901.

(21) Seshadri, R. Lone Pairs in Insulating Pyrochlores: Ice Rules and High-k Behavior. *Solid State Sciences* **2006**, *8*, 256–266.

(22) Henderson, S. J.; Shebanova, O.; Hector, A. L.; McMillan, P. F.; Weller, M. T. Structural Variations in Pyrochlore-Structured $Bi_2Hf_2O_7$, $Bi_2Ti_2O_7$ and $Bi_2Hf_{2-x}Ti_xO_7$ Solid Solutions as a Function of Composition and Temperature by Neutron and X-ray Diffraction and Raman Spectroscopy. *Chemistry of Materials* **2007**, *19*, 1712–1722.

(23) Esquivel-Elizondo, J. R.; Hinojosa, B. B.; Nino, J. C. $Bi_2Ti_2O_7$: It Is Not What You Have Read. *Chemistry of Materials* **2011**, *23*, 4965–4974.

(24) Shirane, G.; Pepinsky, R. Dielectric, X-Ray, and Optical Study of Ferroelectric $Cd_2Nb_2O_7$ and Related Compounds. *Physical Review* **1953**, *92*, 504.

(25) Jona, F.; Shirane, G.; Pepinsky, R. Dielectric, X-Ray, and Optical Study of Ferroelectric $Cd_2Nb_2O_7$ and Related Compounds. *Physical Review* **1955**, *98*, 903–909.

(26) Buixaderas, E.; Kamba, S.; Petzelt, J.; Savinov, M.; Kolpakova, N. N. Phase Transitions Sequence in Pyrochlore $Cd_2Nb_2O_7$ Studied by IR Reflectivity. *Phase Transitions* **2001**, *16*, 9–16.

(27) Kolpakova, N. N.; Waplak, S.; Bednarski, W. EPR Spectroscopy and Optical Microscopy Study of Ferroic States in Pyrochlore. *Journal of Physics Condensed Matter* **1998**, *10*, 9309–9316.

(28) Kolpakova, N. N.; Syrnikov, P. P.; Lebedev, A. O.; Czarnecki, P.; Nawrocik, W.; Perrot, C.; Szczepanska, L. 2-5 Pyrochlore Relaxor Ferroelectric $Cd_2Nb_2O_7$ and its Fe^{2+}/Fe^{3+} Modifications. *Journal of Applied Physics* **2001**, *90*, 6332–6340.

(29) Tachibana, M.; Kawaji, H.; Atake, T. Calorimetric Investigation of Successive Phase Transitions in $Cd_2Nb_2O_7$. *Physical Review B* **2004**, *70*, 064103.

(30) Salaev, F. M.; Kamzina, L. S.; Krainik, N. N. Improper Ferroelectric Phase Transition in Cadmium Pyroniobate. *Soviet Physics–Solid State* **1992**, *34*, 982–985.

(31) Küster, A.; Ihringer, J.; Limper, W.; Wroblewski, T.; Prandl, W. Symmetry of the Ferroelectric Phases of the Pyrochlore $Cd_2Nb_2O_7$ - A Study using a Very High Resolution Powder Diffractometer at a Synchrotron Radiation Source. *Materials Science Forum* **1991**, *79-82*, 791–796.

(32) Smolenskii, G. A.; Salaev, F. M.; Kamzina, L. S.; Krainik, N. N.; Dorogovtsev, S. N. The Investigation of Successive Phase Transitions in Cadmium Pyroniobate Crystal. *Soviet Technical Physics Letter* **1983**, *10*, 253.

(33) Ye, Z. G.; Kolpakova, N. N.; Rivera, J.-P.; Schmid, H. Optical and Electric Investigations of the Phase Transitions in Pyrochlore $Cd_2Nb_2O_7$. *Ferroelectrics* **1991**, *124*, 275–280.

(34) Taniguchi, H.; Shimuzi, T.; Kawaji, H.; Atake, T.; Itoh, M.; Tachibana, M. Ferroelectric Phase Transition of $Cd_2Nb_2O_7$ Studied by Raman Scattering. *Physical Review B* **2008**, *77*, 224104.

(35) Fischer, M.; Malcherek, T.; Bismayer, U.; Blaha, P.; Schwarz, K. Structure and Stability of $Cd_2Nb_2O_7$ and $Cd_2Ta_2O_7$ Explored by Ab Initio Calculations. *Physical Review B* **2008**, *78*, 014108.

(36) Malcherek, T.; Bismayer, U.; Paulmann, C. The Crystal Structure of $Cd_2Nb_2O_7$): Symmetry Mode Analysis of the Ferroelectric Phase. *Journal of Physics Condensed Matter* **2010**, *22*, 205401.

(37) Tachibana, M.; Fritsch, K.; Gaulin, B. D. X-ray Scattering Studies of Structural Phase Transitions in Pyrochlore $Cd_2Nb_2O_7$. *Journal of Physics Condensed Matter* **2013**, *25*, 435902.

(38) Smolenskii, G. A.; Krainik, N. N.; Trepakov, V. A.; Babinsky, A. V. Photoluminescence and Carrier Drift Mobility at the Ferroelectric Phase Transitions. *Ferroelectrics* **2011**, *26*, 835–838.

(39) Lukaszewicz, K.; Pietraszko, A.; Stepie-Damm, J.; Kolpakova, N. Temperature Dependence of the Crystal Structure and Dynamic Disorder of Cadmium in Cadmium Pyroniobates $Cd_2Nb_2O_7$ and $Cd_2Ta_2O_7$. *Materials Research Bulletin* **1994**, *29*, 987–992.

(40) Weller, M. T.; Hughes, R. W.; Rooke, J.; Knee, C. S.; Reading, J. The Pyrochlore Family – A Potential Panacea for the Frustrated Perovskite Chemist. *Dalton Transactions* **2004**, *41*, 3032–3041.

(41) Moisan, J.-Y.; Pannetier, J.; Lucas, J. Cadmium and Lead Antimonates: Some Substitutions. *Comptes Rendus des Seances l'Academie des Sciences et Serie C Science Chimie* **1970**, *271*, 402.

(42) Bernard, D.; Pannetier, J.; Lucas, J. $Hg_2M_2F_6S$ et $Hg_2M_2F_6O$: Deux Nouvelles Familles de Pyrochlores contenant du Mercure et des Metaux M de Transition Divalents. *Solid State Communications* **1975**, *334*, 328.

(43) Le Bail, A. Whole Powder Pattern Decomposition Methods and Applications: A Retrospection. *Powder Diffraction* **2005**, *20*, 316–326.

(44) Rietveld, H. M. A Profile Refinement Method for Nuclear and Magnetic Structures. *Journal of Applied Crystallography* **1969**, *2*, 65–71.

(45) Larson, A. C.; Von Dreele, R. B. General Structure Analysis System (GSAS). *Los Alamos National Laboratory Report* **1994**, *LAUR*, 89–748.

(46) Toby, B. H. EXPGUI , A Graphical User Interface for GSAS. *Journal of Applied Crystallography* **2001**, *34*, 210–213.

(47) Momma, K.; Izumi, F. VESTA 3 for Three-Dimensional Visualization of Crystal, Volumetric and Morphology Data. *Journal of Applied Crystallography* **2011**, *44*, 1272–1276.

(48) Aroyo, M. I.; Perez-Mato, J. M.; Orobengoa, D.; Tasci, E.; de la Flor, G.; Kirov, A. Crystallography online: Bilbao Crystallographic Server. *Bulgarian Chemical Communications* **2011**, *43*, 183–197.

(49) Aroyo, M. I.; Perez-Mato, J. M.; Capillas, C.; Kroumova, E.; Ivantchev, G., S.and Madariaga; Kirov, A.; Wondratschek, H. Bilbao Crystallographic Server I: Databases and crystallographic computing programs. *Zeitschrift fur Kristallographie* **2006**, *221*, 15–27.

(50) Aroyo, M. I.; Kirov, A.; Capillas, C.; Perez-Mato, J. M.; Wondratschek, H. Bilbao Crystallographic Server II: Representations of crystallographic point groups and space groups. *Acta Crystallographica* **2006**, *A62*, 115–128.

(51) O'Keefe, M. EUTAX. Ph.D. thesis, Arizona State University, 1992.

(52) Kresse, G.; Furthmuller, J. Efficient Iterative Schemes for Ab Initio Total-Energy Calculations using a Plane-Wave Basis Set. *Physical Review B - Condensed Matter and Materials Physics* **1996**, *54*, 11169–11186.

(53) Joubert, D. From Ultrasoft Pseudopotentials to the Projector Augmented-Wave Method. *Physical Review B - Condensed Matter and Materials Physics* **1999**, *59*, 1758–1775.

(54) Perdew, J. P.; Ruzsinszky, A.; Csonka, G. I.; Vydrov, O. A.; Scuseria, G. E.; Constantin, L. A.; Zhou, X.; Burke, K. Generalized Gradient Approximation for Solids and their Surfaces. *arXiv:0707.2088* **2007**, *136406*, 1–4.

(55) Blochl, P. E. Projector Augmented-Wave Method. *Physical Review B* **1994**, *50*, 17953–17979.

(56) Campbell, B. J.; Stokes, H. T.; Tanner, D. E.; Hatch, D. M. ISODISPLACE: A Web-Based Tool for Exploring Structural Distortions. *Journal of Applied Crystallography* **2006**, *39*, 607–614.

(57) Orobengoa, D.; Capillas, C.; Aroyo, M. I.; Perez-Mato, J. M. AMPLIMODES: Symmetry-Mode Analysis on the Bilbao Crystallographic Server. *Journal of Applied Crystallography* **2009**, *42*, 820–833.

(58) Perez-Mato, J. M.; Orobengoa, D.; Aroyo, M. I. Mode Crystallography of Distorted Structures. *Acta Crystallographica Section A* **2010**, *66*, 558–590.

(59) Bernard, D.; Le Montagner, S.; Pannetier, J.; Lucas, J. Un Nouveau Compose Ferroelectrique $Cd_2Nb_2O_6S$. *Materials Research Bulletin* **1971**, *6*, 75–80.

(60) Matthias, B. T. New Ferroelectric Crystals. *Physical Review* **1949**, *75*, 1771.

(61) Cohen, R. E. Origin of Ferroelectricity in Perovskite Oxides. *Nature (London)* **1992**, *358*, 136.

(62) Cohen, R. E.; Krakauer, H. Electronic Structure Studies of the Differences in Ferroelectric Behavior of $BaTiO_3$ and $PbTiO_3$. *Ferroelectrics* **1992**, *136*, 65.

(63) Sleight, A. W.; Bierlein, J. D. Phase Transition in $Cd_2Ta_2O_7$ and the $Cd_2Nb_{2-x}Tax O_7$ Series. *Solid State Communications* **1976**, *18*, 163–166.

(64) Song, Y. M.; Dai, J. Q.; Zhang, H. First principles studies of the phonon, polarization, dielectric and piezoelectric responses of pyrochlore Cd2Nb2O7. *Ferroelectrics* **2015**, *478*, 106–117.

(65) Pannetier, J. La Structure Pyrochlore: Approche Theorique un Modele D'energie de Reseau - Nouveaux Materiaux. Ph.D. thesis, University of Rennes, 1974.

(66) Shannon, R. D.; Prewitt, C. T. Effective Ionic Radii in Oxides and Fluorides. *Acta Crystallographica Section B: Structural Crystallography Crystal Chemistry* **1969**, *25*, 925–946.

(67) Walsh, A.; Watson, G. W. Polymorphism in Bismuth Stannate: A First-Principles Study. *Chemistry of Materials* **2007**, *19*, 5158–5164.

(68) Lewis, J. W.; Payne, J. L.; Evans, I. R.; Stokes, H. T.; Campell, B. J.; Evans, J. O. An Exhaustive Symmetry Approach to Structure Determination: Phase Transitions in $Bi_2Sn_2O_7$. *Journal of the American Chemical Society* **2016**, *138*, 8031–8042.

(69) Reading, J.; Knee, C. S.; Weller, M. T. Syntheses, Structures and Properties of some Osmates(IV,V) Adopting the Pyrochlore and Weberite Structures. *Journal of Materials Chemistry* **2002**, *12*, 2376–2382.

(70) Brews, J. R. Energy Band Changes in Perovskites due to Lattice Polarization. *Physicsal Review Letters* **1967**, *18*, 662–664.

Graphical TOC Entry